

Long-slit imaging dual order spectrograph – LIDOS

Stephan Robert McCandliss, Kevin France, Paul Feldman and Russ Pelton ^a

^aThe Johns Hopkins University Department of Physics and Astronomy
3400 North Charles Street
Baltimore, Maryland 21218 USA

ABSTRACT

We report on the design and fabrication of a long-slit imaging dual order spectrograph to be launched on a sounding rocket-borne telescope. The instrument's purpose is to investigate faint emissions of extended astronomical regions near bright objects on intermediate angular scales ($3 - 300''$) and with moderate spectral resolution ($\approx 3 \text{ \AA}$) in the $900 - 1650 \text{ \AA}$ bandpass. The design relies upon a toroidally figured holographically ruled grating to provide astigmatism correction in both orders and an intrinsically low scattered light level. The use of both orders doubles the collection efficiency, nearing that achievable with a blazed grating, while simultaneously providing a system redundancy that is desirable in the high risk environment of space-based astronomy missions. We will discuss the predicted instrument performance and present preliminary pre-flight calibration data.

Keywords: spectroscopy, far-ultraviolet, grating, calibration, optomechanical design

1. INTRODUCTION

The angular extent and spectral content of the myriad nebulae found in space provide us with the diagnostic fingerprints from which we define distinct morphological classes such as, supernova remnants, planetary nebulae, reflection nebulae, debris disks, translucent clouds, giant molecular clouds, globular clusters, starbursts, galaxies, and quasars. This is the primary business of astronomy; to sift photons on ever finer spectral and angular scales, over as wide a bandpass as possible, and then define reductionist criteria. Spectro-spatial observations allow us to assay the chemical composition of the nebular material, determine its physical state, and investigate the dynamics of its interaction with local energy sources. The far-UV provides a number of unique molecular and atomic spectral signatures for the presence of H_2 , CO , HI , $\text{C I} - \text{C IV}$, $\text{N I} - \text{N V}$, O I , O III , O V , O VI , and $\text{S I} - \text{S VI}$, and hence is valuable for probing the composition over a wide range of energetic environments.

Observations of nebulae surrounding very bright point sources present special problems. To follow the dissipation of energy from the bright object into the surrounding matter requires instrumentation with a high enough dynamic range to simultaneously detect both the dim and bright emissions. The low level sensitivity of any instrument is set by the scattered light in the optical system and background counts in the detector, which together comprise the background equivalent flux (BEF) that unavoidably adds to the source signal. Background subtraction always degrades the signal-to-noise ratio (s/n) of the source signal, thereby increasing the time required to reach a desired s/n. This degradation is especially pronounced when the source signal is of order or less than the BEF. Optics with low scattered light properties and detectors with low background counts are desired when making such low flux measurements. The high flux limit is set by the detector saturation point where the detector becomes non-linear (or non-proportionate) in its response to a signal.

It is difficult to find a single detector that has both a low detector background and a high saturation limit. Photoemissive detectors, like microchannel plates (MCP), are capable of counting individual photons, but suffer deadtime correction and microchannel charge depletion effects at high count rates. Photoconductive detectors, like charge coupled devices (CCD) have a linear response up to the pixel full well limit but, at the low end they have the ever present read noise and typical dark count rates two orders of magnitude higher than photoemissive devices, even when cooled to 200 K.

To take advantage of the complimentary properties of photoemissive and photoconductive detectors for addressing this class of problems we have designed a long-slit imaging dual order spectrograph (LIDOS). Herein we will describe

S.R.M. email: stephan@pha.jhu.edu, Telephone: 1 410 516 5272

design considerations for the spectrograph, its configuration, its subsystems, its telescope, various component calibrations undertaken to date, and our expected long-slit spectral performance and sensitivity limits. This instrument will be flown on a sounding rocket preliminarily scheduled for mid-2003. Several follow-up flights are also planned to acquire long-slit spectra of a sampling of extended nebulae and star formation regions. The general science goal is to determine the degree to which absorption and scattering by dust regulates the far-UV radiation field and protects molecules from photodestruction. We also seek to understand the relationship between dust and fluorescent molecular hydrogen as pumped by local sources of far-UV radiation. These sounding rocket flights are intended to validate the dual-order spectrograph concept and enable its use on long duration missions studying faint or extended sources at spectral and spatial resolution scales complementary to the capabilities of *FUSE*, and the *HST* spectrographs STIS and COS.

2. INSTRUMENT

Our scientific program to study dust and molecular hydrogen in the vicinity of bright targets requires a long-slit spectrograph with good off-axis imaging, low scattered light and high dynamic range, covering the 900–1650 Å bandpass spanned by fluorescent molecular hydrogen emission. The instrument design is described here and the parameters are summarized in Table 1. The spectrograph and telescope are shown in Figure 1.

2.1. Dual Order Grating

We have chosen a Rowland circle mounting with a holographically ruled grating, straight rulings and a toroidal figure for our dispersing element. The single bounce of the concave grating in a Rowland circle mount is the most efficient dispersion method in the far-UV, where optical components with efficiencies of 50% are considered excellent. The need for low scatter is met through the use of a holographically ruled grating; generally recognized to have ~ 10 times lower scattered light than a conventionally ruled blazed grating.^{1,2} The holographic etching process tends to produce a groove with a symmetric profile, the consequence of which is to yield equal power in both positive and negative orders.³ A dual-order configuration is most easily realized with a normal incidence mount ($\alpha = 0^\circ$), which diffracts the positive and negative orders symmetrically about the grating normal. This mounting also reflects the grating zero-order back through the entrance slit, greatly reducing the available undispersed long wavelength light within the housing that might scatter into the detectors.

A concave grating with a spherical figure suffers from astigmatism, the reduction of which is crucial to achieving good spatial resolution and low BEF. One method of eliminating astigmatism is to use a toroidal figure with a slightly smaller radius perpendicular to the dispersion direction, which causes the sagittal and tangential foci to coincide at a particular wavelength, 1275 Å in our design. Astigmatism is also reduced significantly throughout the bandpass in comparison to a spherical grating. Astigmatism correction with a toroidal figure has the advantage of being independent of the sign of the order. The other common means of astigmatism reduction, the use of curved rulings on a spherical substrate (most easily achieved with a holographic process), does depend on the sign of the order. The consequence of this dependence is to correct the astigmatism in one order while doubling it in the other. This can be demonstrated by examining the holographic astigmatism aberration coefficients for a concave grating.⁴ We have recently purchased from Jobin-Yvon a toroidal figured grating with straight rulings, holographically etched into a CVD-SiC substrate. The parameters of the grating are given in Table 1. Efficiency measurements are discussed in §3.

2.2. Detectors

MCP: Our photon counting detector is a windowless microchannel plate (MCP) Z-stack with a double delay-line anode.⁵ It is a commercial-off-the-shelf product built by Sensor Sciences, offering low image distortion, low fixed pattern noise, high operational stability and environmental robustness. Delay-line MCP's are used on a number of spacebased imaging and spectroscopic missions.^{6–9} Ours was originally used to acquire long-slit UV spectra of Comet Hale-Bopp.¹⁰ The delay line anode and detector body are attached to a vacuum baseplate, containing four signal and one high voltage feedthrough. A preamplifier is mounted on the back of the vacuum flange to provide a common ground. An opaque CsI photocathode is expected to provide a quantum detection efficiency (QDE) of between 15 – 45% throughout the bandpass. The active area is 30 mm \times 12 mm with a 1 mm wide occulting strip in the center to provide for a spectro-coronagraphic mode on bright continuum sources. The specified detector resolution of 30 μ m FWHM in X (dispersion direction) and 50 μ m FWHM in Y (cross-dispersion direction) comfortably exceed the pointing limited spectral and spatial resolution goals (3 Å and 3"). The detector is very quiet with a laboratory background rate of (0.5 cnts s⁻¹ cm⁻²).

Table 1. Instrument Summary	
Telescope, f/16 Dall-Kirkham	
Clear Area	1064 cm ²
Diameter	393 mm
Plate Scale	32.''8 mm ⁻¹
Primary Mirror Substrate	Zerodur
Primary Mirror Coating	IBS-SiC
Secondary Mirror	CVC-SiC
Spectrograph, Dual Order Rowland ($\alpha=0^\circ$)	
Grating Ruling	Holographic
Grating Figure	Toroidal
Grating Material	CVD-SiC
Wavelength range	900–1650 Å
Stigmatic Wavelength	1275Å
Rowland Circle Diameter	600 mm
Ruling Density	700 lines mm ⁻¹
Dispersion	25.9 Å mm ⁻¹
Slit size	10'' × 300''
Slitjaw FOV	20' Diameter
MCP Open-window	
CsI Cathode 900 – 1650 Å	QDE = 45 – 15%
Pulse Location Anode	Double Delay-line
Active area	30 mm × 12 mm
Pixel format	2048 × 512
Resolution X (spectral)	< 30 μm
Resolution Y (spatial)	< 50 μm
Maximum countrate	10 ⁴ counts s ⁻¹
Background rate	≈ 1.5 e ⁻ cm ⁻² s ⁻¹
CCD, Open-window thinned δ-doped SiTe ST-001A	
QDE 900–1650Å	40% (estimated)
Pixel Size	24μm
Pixel Format	1100 × 330
Active area	26.4mm × 7.9mm
Dark Rate @ -85°C	400 e ⁻ cm ⁻² s ⁻¹
Intrinsic Resolutions	
Spectral	1.1 – 1.7 Å
Spatial	1'' – 3.''5
Pointing Limited Resolution (2.5'' jitter)	
Spectral (2.5'' jitter)	3.0 – 3.5 Å
Spatial (2.5'' jitter)	2.''7 – 4.''4
Instantaneous FOV	Ω=1. × 10 ⁻⁹ sr
Peak Summed Effective Area : ~16 cm²	

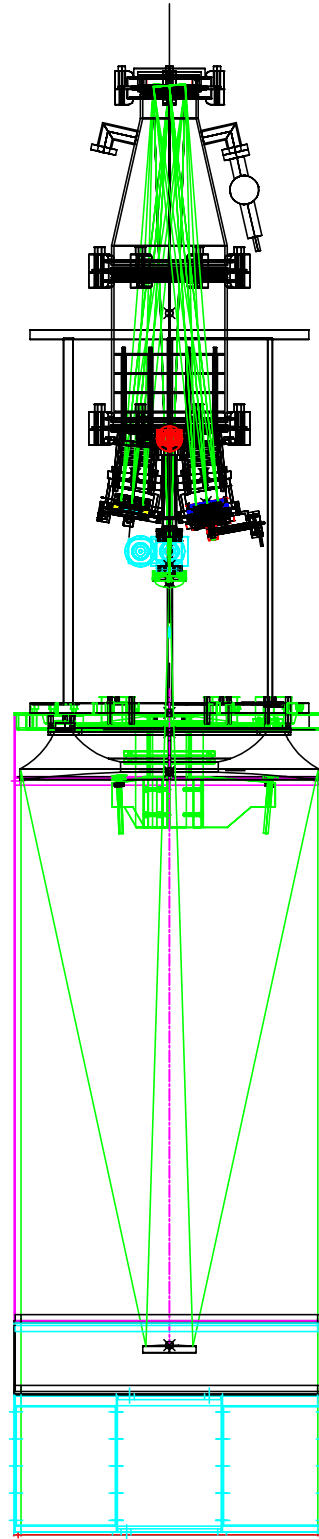


Figure 1. The telescope and spectrograph.

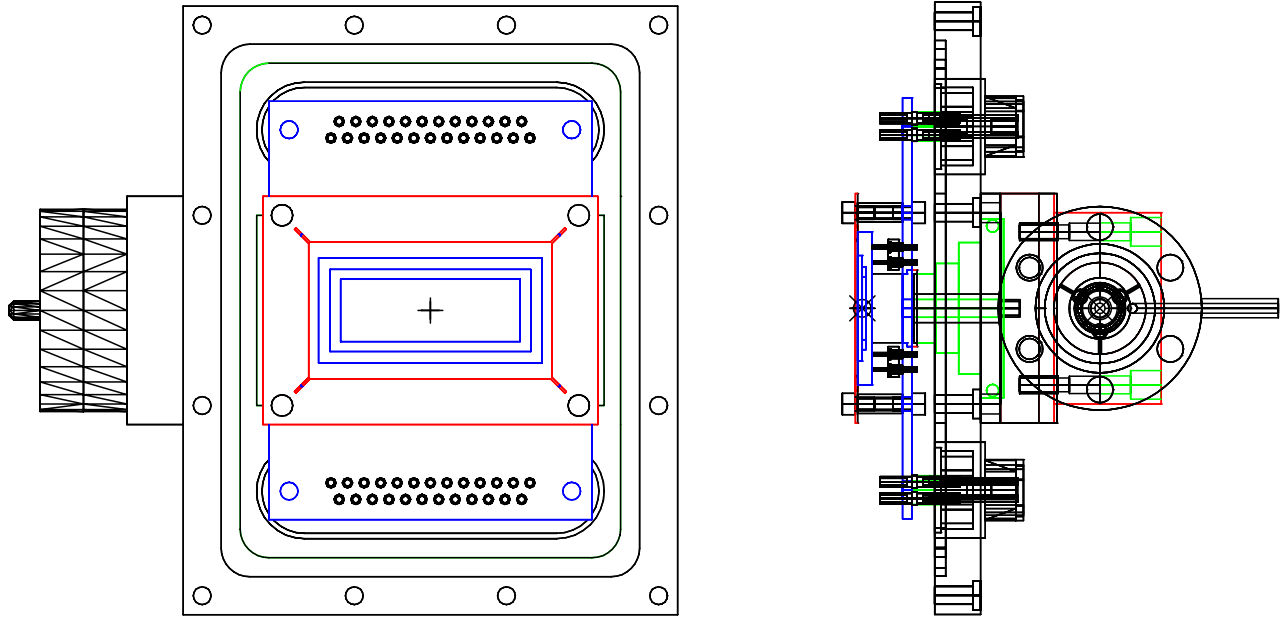


Figure 2. Two views of the CCD mounted on its cryo package.

δ -doped CCD: To accommodate stars brighter than $\approx 3 \times 10^{-11}$ ergs cm^{-2} s^{-1} \AA^{-1} we require a UV sensitive CCD. The sensitivity of untreated CCDs at wavelengths below 4000 \AA falls to zero because the absorption length of UV photons in silicon can be as short as 4 nm. Photon generated electrons become trapped and annihilated in a positive surface potential well that forms in the native oxide/silicon interface. A number of methods for creating a negative charge at the interface to eliminate the problematic attractive potential well have been demonstrated.¹¹ We have used an air-soak, UV-flood and cool technique to achieved a relatively flat 45% QDE (with a quantum yield of $\approx 2 e^-$ photon $^{-1}$) from 1175 to 1608 \AA on thinned non-AR coated SiTe chips.¹² The QDE below 1175 \AA is expect to be similar.

The air-soak and UV-flood and cool technique requires repeated vacuum cycling, and constant cooling to maintain UV sensitivity. These are impractical requirements for our application. Fortunately a stable and permanent backside charge treatment for thinned CCD's exists in the form of the δ -doped process.¹³ Molecular beam epitaxy (MBE) is used grow a permanent δ -function type repulsive potential profile on the CCD backside to repell UV photo-generated electrons in to the charge collection wells. UV QDE is found to be uniform and stable to thermal cycling and illumination history. QDE measurements at Stanford Synchrotron Radiation Laboratory (SSRL) covering the wavelength range from 60 to 1500 \AA ^{14,15} are in agreement with those achieved by the air-soak, UV-flood method.¹²

We have acquired a JPL δ -doped SiTe ST-001A CCD that has a format of 1100×330 , $(24 \mu\text{m})^2$ pixels. A combination vacuum flange, signal feedthrough, and cryogenic cooling package has been developed to mount the CCD to the spectrograph. The vacuum flange utilizes the same footprint as the MCP detector, to allow for convenient future reconfigurations. The flange material is an oxygen free copper and 316 stainless steel (SS) bi-metal, which was bonded together by an explosive welding process. Twin hermetic 25 pin subminiature D-type connectors are welded to the SS portion of this rectangular vacuum flange. A pocket milled through the SS uncovers the copper that serves as the heatsink to a 4 stage thermoelectric cooler (TEC). The heatsink is kept at a constant temperature by a Joule-Thompson cooler attached to the outside of the flange.

The cold end of the TEC is compressed by a copper coldsink mounted in the center of a CCD headboard, trapping it against the flange heatsink. A calibrated thermistor is mounted in the copper coldsink. The CCD sits in a pair of double row "SIPS" strips mounted to the headboard on either side of the coldsink. The CCD is compressed against the coldsink with a rectangular spring, mounted on standoffs atop the headboard. Electrical traces run from the SIPS strips directly to D-type socket arrays at the ends of the headboard. The whole headboard assembly plugs directly into the D-connectors on the flange. It is held in place on standoffs attached to the D-connector screw mounts. Provision has also been made for

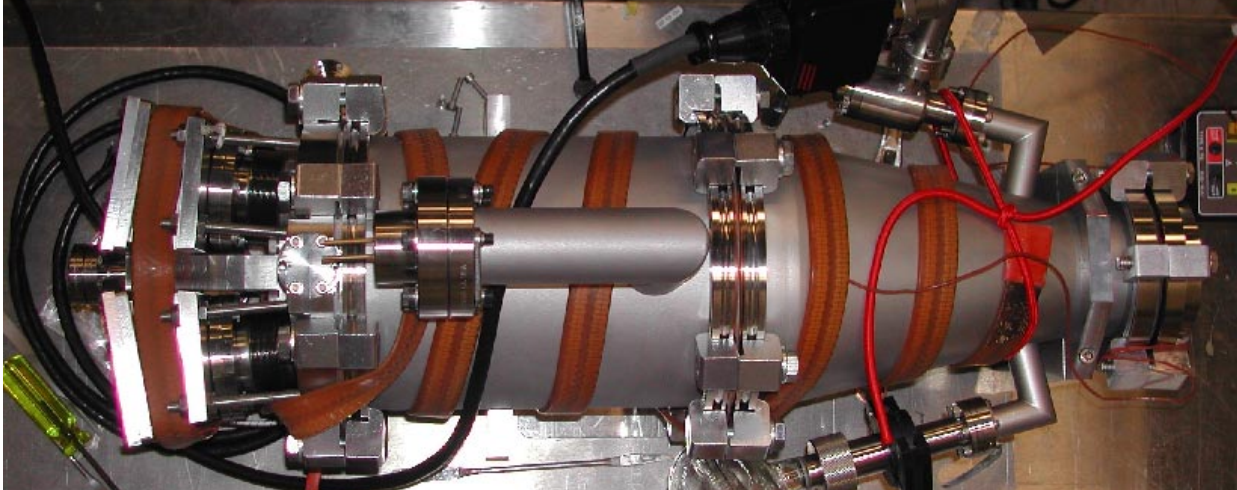


Figure 3. LIDOS housing assembled for preliminary vacuum bakeout.

the attachment of the TEC and thermistor leads to the headboard. All CCD electronics are mounted outside the vacuum in close proximity to the flange. A schematic of the CCD and mounting flange is shown in Figure 2. This mounting and cryogenic scheme will be tested in the coming months.

2.3. Spectrograph Mechanical Structure

We have chosen a slightly off Rowland circle mounting for the spectrograph to relieve crowding of the detectors and slitjaw. The detectors have been moved inward and the slit outward from their nominal positions on the Rowland circle. The consequence is to demagnify the spectrograph image plane about 15%. The spectrograph structure is a vacuum vessel evacuated to pressure of $\approx 10^{-8}$ Torr, providing contamination control for the grating and detectors during storage and testing of the instrument. The vacuum is maintained by a 50 litre s^{-1} non-evaporable getter pump. A ruggedized 2 litre s^{-1} vac-ion pump serves primarily as a pressure gauge. The spectrograph structure, sitting atop the telescope, consists of three main parts as shown in Figure 1 and Figure 3.

At the top is a conical reducer with a modified NW 80 iso-flange for mounting the grating at one end. It has a standard NW 160 iso-flange at the other end. This reducer has angled mini-conflat flange (cff) ports for attaching a pumpout valve and the vac-ion pump. In the middle, attached to the large end of the reducer, is an NW 160 iso-nipple with an angled 2.75 inch cff for mounting the getter pump. The reducer and nipple are commercial-off-the-shelf parts slightly modified by the vendor. At the bottom, attached to the base of the 160 nipple, is a custom designed detector baseplate that holds the detector bodies at the proper angle with respect to the diffracted beams. The detector bodies attach to the baseplate by compliant welded bellows to allow for focus adjustment. Situated between the two detectors is a 2.25 inch to mini-cff reducer for mounting a gatevalve that serves as the spectrograph entrance aperture seal and is the mount point for the slitjaw. The slitjaw, located in the focal plane of the telescope, consists of a mirrored plate into which a long-slit has been cut to define the entrance aperture of the spectrograph. It is angled to pass the image of the field surrounding the slit to a tracking camera to aid the target acquisition process. Light baffles for defining the focal ratio of the input and diffracted beams are attached on the vacuum side of the detector baseplate. A normally opened shutter is planned to be mounted to one of the baffles in front of the CCD to allow clearing the array before an exposure and for smear free readout afterwards.

2.4. On-board Far-UV Electron Impact Calibration Lamp

Calibration spectra of emission line and continuum sources are essential to characterizing the performance of spectroscopic instrumentation and have long been utilized to improve science return at longer wavelengths. It is standard astronomical practice to acquire concomitant calibration spectra for processing with the object spectrum. Spectra of emission line and continuum sources provide a means to monitor instrumental stability and account for variations in the wavelength scale and detector flat-field within the spectral reduction process.

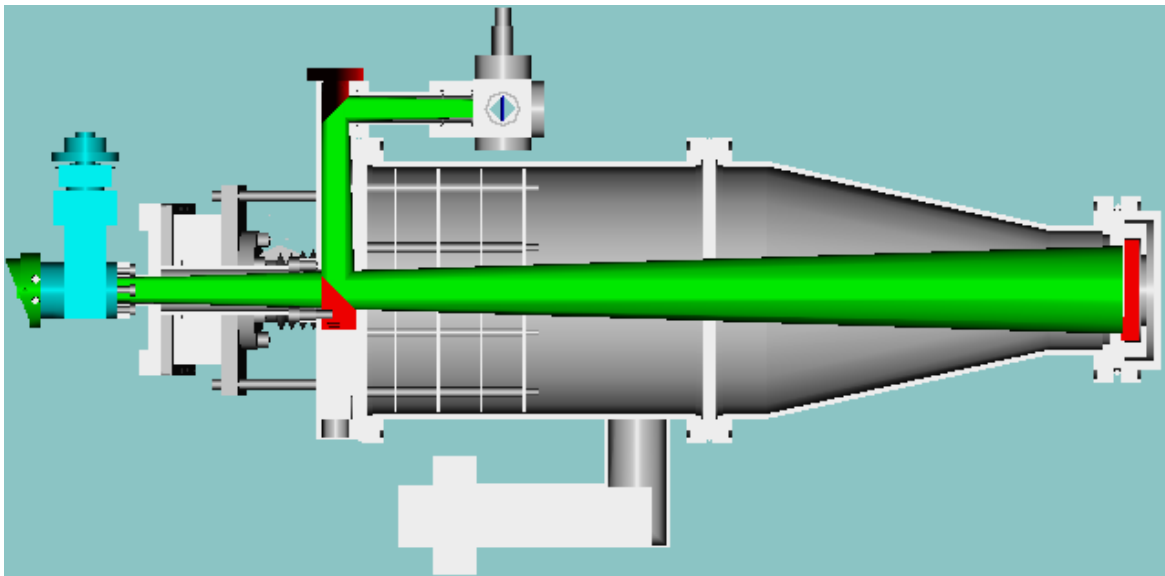


Figure 4. Cutway shows the optical path of the electron impact calibration lamp and the telescope input in green. The tungsten target is shown in blue. The pickoff flats and grating are shown in red.

Compact sources for use in the far-UV have long been desired. We have found that an electron impact source can be used to produce both emission lines, and a bremsstrahlung continuum in the far-UV.¹⁶ This source has an advantage over coronal discharge lamps as it can be used within an ambient vacuum compatible with microchannel plate operation. In operation, current flowing through a filament provides a source of free electrons that are accelerated towards a tungsten target by an applied voltage. Electrons impacting with residual gas molecules produce line emissions characteristic of the excited fragments. Electrons impacting the target will produce the bremsstrahlung.

Our electron impact lamp consists of a mini-cff cube into which are mounted the filament in proximity to a tungsten target rod 3/32 inches in diameter. In operation we find the electron emission current is a strong function of filament current (temperature) and target bias voltage, but is only somewhat dependent on gas pressure. Emission current increases sharply as the filament temperature goes above > 1100 K. The contrast between emission lines and bremsstrahlung can be decreased by increasing the target bias voltage. This effect is due in part to the increase in bremsstrahlung emission with increasing emission current. It is also contributed to by the decrease in line emission strength, per unit electron emission current, as a function of increasing electron impact energy. This is the expected trend for electron impact excitation of molecules where the cross-sections typically rise to a peak at 50 – 100 eV and then fall towards higher electron energies.¹⁷⁻²² Our source follows this trend even though the energy of electrons in the line emitting volume is not mono-energetic. In principal, knowledge of the residual gas content, the volumetric distribution of electrons in the residual gas excitation region and the electron impact excitation cross-sections could allow this lamp to be used as an absolute calibration standard as has been done with mono-energetic sources.²³ The atomic and molecular emission lines present will depend upon the quality of the vacuum. They result from the electron impact dissociation of H_2O , N_2 and to a lesser degree, H_2 , CO_2 , and CO . Typically lines of H I Lyman- α , N I $\lambda 1200$, N II $\lambda 1084$, O I $\lambda 1304$, O I $\lambda 989$, and N_2 (c'_4 -X) 958 dominate, while Lyman- β , O I $\lambda 1152$, N I $\lambda 1243$, N I $\lambda 1135$, C II $\lambda 1335$, CO (B-X) 1150 and CO (C-X) 1088 are weaker.

The side view in Figure 4 shows the layout of the electron impact lamp with its two flat pick off mirrors within the LIDOS housing. An entrance slit for the lamp is mounted in the copper gasket in the flange joining the lamp to spectrograph. A deep channel running the diameter of the baseplate allows for the propagation of a beam from the lamp slit into an optical path intercepting the grating and detectors. Both mirrors are made from polished SS and overcoated with ion beam sputtered SiC. The first is a simple 45° elliptical flat. The second, located along the telescope optical axis, has a horseshoe shaped cutout to allow an unobstructed passage of the telescope beam, while picking off the faster calibration beam and redirecting it towards the grating.

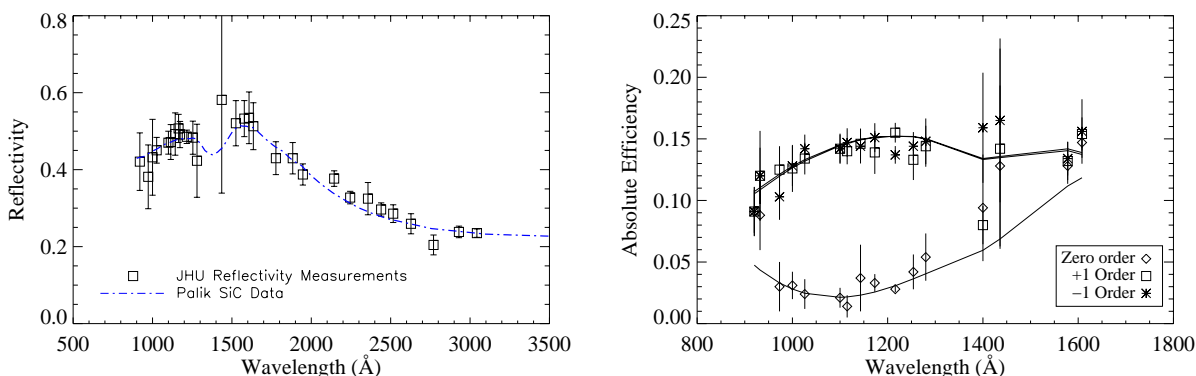


Figure 5. On the left we show the reflectivity of a Trex Enterprises CVC-SiC sample substrate. The solid line is a calculation of the SiC reflectivity from optical constants in the literature. On the right we show the measured absolute efficiency of Jobin-Yvon CVD-SiC Grating. The solid lines are fits to the efficiency of the three orders assuming the calculated SiC efficiency shown on the left degraded by an overall scale factor of 0.9.

2.5. Telescope and Far-UV Coatings

Although prime focus spectroscopic designs are inherently more efficient their off axis imaging performance is poor. Good off-axis imaging is best achieved with a Cassegrain telescope and this consideration outweighs the efficiency lost in the extra bounce. However, a prime focus telescope tends to have a faster focal ratio than a Cassegrain. Consequently the spectrograph astigmatism is correspondingly higher, increasing its BEF (see § 4). Hence the lower efficiency of the Cassegrain is mitigated by a lower BEF and such a system can ultimately be more sensitive, albeit at the expense of longer exposure times.

We use the Dall-Kirkham Cassegrain configuration where the primary is elliptical and the secondary spherical. The primary mirror is coated with a layer of ion-beam sputtered SiC (IBS-SiC) over Al. The Al provides much higher visible reflectivity than bulk SiC, which is necessary for the visible sensitive tracking camera. Our experience has shown that aged IBS-SiC has a lower reflectivity ($\approx 30 - 35\%$) than chemical vapor deposited (CVD) SiC ($\approx 40 - 50\%$).²⁴ It is less costly to coat a large conventionally figured zerodur substrate with IBS-SiC than it is to make one from CVD-SiC.²⁵ This technology has been successfully employed by HUT on *Astro-2* to triple its effective area relative to *Astro-1*²⁶ and by *FUSE* to shift from costly grazing incidence optics to a less expensive normal incidence design.²⁷ However, the small size and spherical shape of the secondary mirror is relatively simple to produce with conventional mirror fabrication techniques even in a substance as hard a SiC. We have secured a flat of chemical vapor composite (CVC) SiC from Trex Enterprises for this purpose. Recent advances in the fabrication of CVC-SiC hold promise for the production of near net shape SiC optics at a fraction of the cost for producing conventional CVD-SiC,²⁸ suggesting the cost effective fabrication of large lightweight SiC mirrors may be possible in the future.

3. SiC REFLECTANCE AND GRATING EFFICIENCY MEASUREMENTS

The JHU Calibration and Test Equipment facility is used to measure mirror reflectance, diffraction grating efficiency, and quantum detection efficiency at vacuum ultraviolet wavelengths, from 584 – 3000 Å.²⁹ The facility uses a combination of lamps and evacuated monochromators to produce an $f/50$ monochromatic beam for these measurements. The experimental setups for measuring mirror reflectance¹² and grating efficiency³ have been described previously. For measurements between $1600 \leq \lambda \leq 3000$ Å we use a 542F type photomultiplier tube with a sapphire window and a Cs₂Te cathode. A 542G tube with a LiF window and a CsI cathode is used for measurements between $1050 \leq \lambda \leq 1600$ Å. For $\lambda \leq 1050$ Å we use a Bi-Alkali 541E tube with a sodium salicylate scintillator to down-convert far-UV photons to the visible. These tubes are positioned to measure the intensity of the light incident on the sample and then moved to measure the intensity of the light reflected from the sample. The ratio is the reflectivity or efficiency of the sample. Between each measurement, the chamber is closed off from the monochromator and a dark value is measured and subtracted from the signal. The standard deviations of the incident, reflected, and dark measurements are recorded and used in the error analysis.

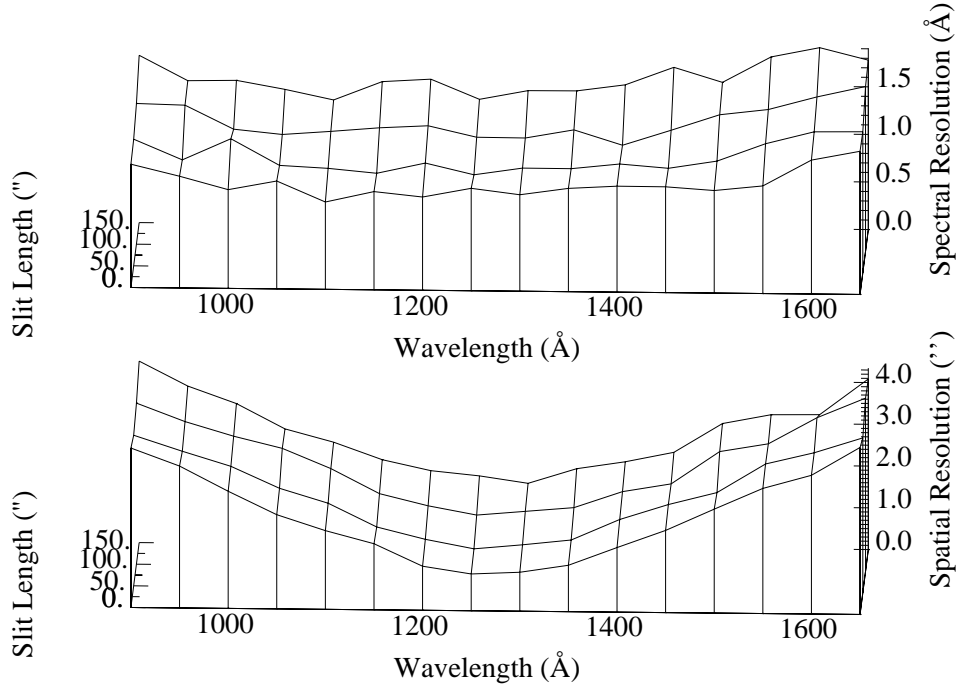


Figure 6. These surface plots, for an input PSF of $1''$, show the variation of spectral (top) and spatial (bottom) resolution as a function of wavelength and distance from slit center.

3.1. Trex CVC-SiC Reflectance

The Trex Enterprises chemical vapor composite (CVC) process is a variant of the chemical vapor deposition (CVD) process but with 10 times the growth rate making it less expensive than the traditional deposition process. The CVC mirror was measured from 900 – 3000 Å in the facility described above. The UV reflectivity measurements shown in Figure 5 on the left are the first of their kind for a SiC substrate produced using the CVC process. The solid line is the reflectance of 6H SiC as calculated from the optical constants listed in the literature.³⁰ The measurements are remarkably consistent with the calculated values.

3.2. JY-Torodial Grating Absolute Efficiency

The absolute efficiency of the JY-Torodial grating was measured by mounting the grating at a fixed angle and rotating the photomultiplier tubes to the appropriate incident and diffracted positions of the grating’s Rowland circle. The incident $f/50$ beam focus was coincident with the grating’s spherical center. Measurements were made of the minus, zero, and plus orders over the bandpass of the instrument, 900 – 1700 Å are shown on the right of Figure 5. The solid lines are fits to the efficiency of the three orders assuming the calculated SiC efficiency shown on the left. The fitting procedure varied the depth of an assumed trapezoidal groove profile along with an overall scale factor for the SiC reflectivity. The steepness of the sides of the trapezoid were then varied until all orders converged on a common depth, which we found to be $\approx 20\%$ larger than specified in Table 1. The sides have slopes $\approx 22.5^\circ$. We found the SiC efficiency scale factor to be 0.9 of the calculated value. All these results are consistent with the expectations of the manufacturer. These fits will be used to model the expected effective area of the instrument in § 4.

4. EXPECTED PERFORMANCE

4.1. Spectral Performance

We have performed a raytrace of the telescope/spectrograph combination, described in the previous sections, with an astigmatism corrected wavelength of 1275 Å. In the raytrace, the telescope point spread function (PSF) was simulated by a $1''$ (FWHM) gaussian object. PSF output by the spectrograph were calculated for wavelengths ranging from 900 to 1650 Å and positions $0''$, $50''$, $100''$, and $150''$ off-axis. The results are summarized in the surface plots shown in Figure 6.

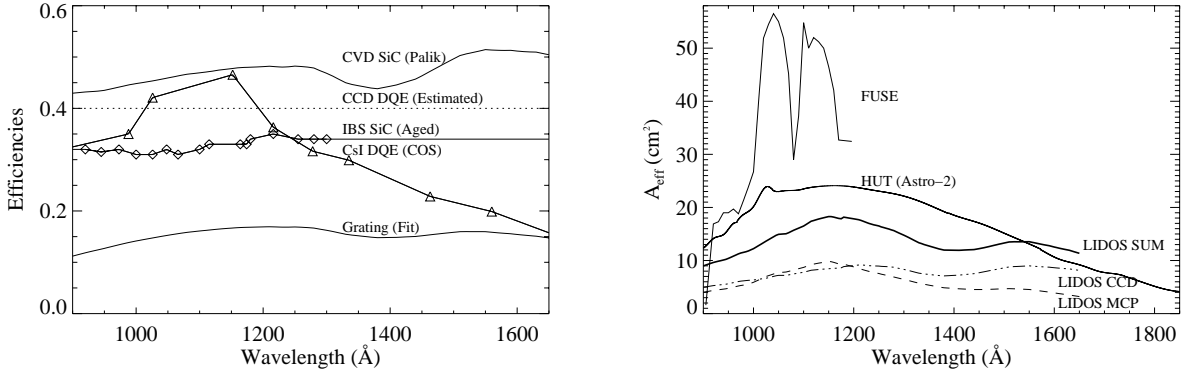


Figure 7. On the left we show the component efficiencies used to estimate the A_{eff} in Figure 7. The lower solid line is the fit to the absolute grating efficiency from Figure 5. The upper solid line is the calculated CVD-SiC reflectivity. The reflectivity of aged IBS-SiC are (\diamond), the QDE of CsI are (\triangle) and the estimated CCD QDE is the dotted line. On the right we show A_{eff} in the MCP (dash) and CCD (dot-dot-dot-dash) channels and the sum of the two channels (thick) compared to *HUT(Astro-2)*, and *FUSE*.

The spectral resolution grows modestly with increasing offaxis position, ranging from 1.1 - 1.7 Å. The spatial resolution shows the effects of astigmatism, yielding output spectral PSFs ranging from 1'' - 4''. As the pointing limit of the sounding rocket is expected to be closer to 2.5'' the spectral resolution will grow accordingly. The dip in the spatial resolution will fill-in and the variation will become less pronounced.

4.2. Effective Area and BEF

The effective area is calculated as

$$A_{eff}(\lambda) = A_t R_p(\lambda) R_s(\lambda) E_g(\lambda) R_g(\lambda) Q_d(\lambda) T_{gr},$$

where A_t is the clear area of the telescope, R_p , R_s and R_g are the reflectivities of the primary mirror, secondary mirror and grating, respectively, E_g is the groove efficiency of the grating, Q_d is the quantum efficiency of the detector, and T_{gr} is the transmission of the ion repeller grids (0.97). The IBS-SiC reflectivity is a measurement of an aged coating on our telescope primary and is fully stabilized. We use the CVD-SiC calculation, shown as the solid line on the left of Figure 5, for the secondary mirror reflectivity. The CsI quantum efficiency, $Q_d(\lambda)$, are from recent measurements of a Cosmic Origins Spectrograph detector, kindly provided by O. H. Siegmund (private communication). The CCD $Q_d(\lambda)$ are estimated at a fixed 44%, consistent with previous experience.¹² The grating absolute efficiency ($E_a = E_g R_g$) is taken from the fit to the data shown on the right of in Figure 5. The individual component efficiencies are shown in Figure 7 on the left. The effective area is shown on the right along with those of the prime focus instruments *FUSE*³¹ and *HUT/Astro-2*.²⁶ The effective areas for the MCP and CCD channels are shown separately as dashed and dot-dot-dot-dashed lines respectively and the summed area as a thick line.

At high count rates the MCP detector linearity is globally limited by the overall speed of our pulse locating electronics to $\approx 10,000$ counts s^{-1} , and locally limited by charge depletion in the micropores of the MCP to ≈ 5 counts channel $^{-1}$ s^{-1} . The maximum count rate in the CCD detector is limited by the full well capacity of a pixel, $\approx 50,000$ counts pixel $^{-1}$, and the minimum shutter time (1 s). Count rate maxima are plotted as straight lines on the left in Figure 8.

The ability to detect a faint source is limited by the spectrograph BEF. This is the signal that lies underneath all spectra that are extracted from the detector. The BEF present in a region around a point source spectrum changes with wavelength because of variations in the astigmatism height, the effective area, and the fall off in the profile of scattered light from geocoronal Lyman- α and other airglow lines. We estimate the BEF for the MCP and CCD channels (in ergs cm^{-2} s^{-1} Å $^{-1}$) with the formula,

$$F_\lambda = \frac{hc}{\lambda} \frac{B(\lambda)}{A_{eff}(\lambda)} \frac{H_{ast}(\lambda)}{D}.$$

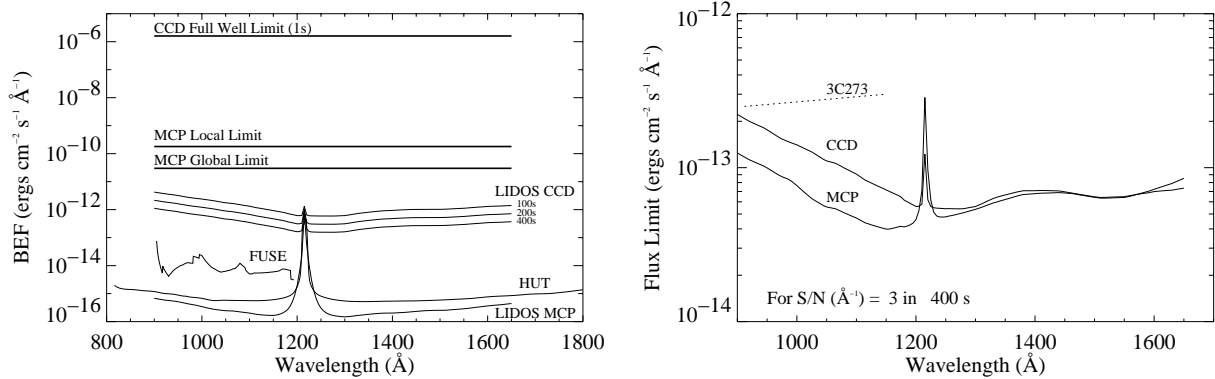


Figure 8. On the left are shown flux maxima (straight lines) and BEF for the CCD and MCP channels (as labeled), compared to *FUSE* and *HUT* (*Astro-2*). The CCD background is shown for integration times of 100, 200, and 400 seconds. On the right are shown the flux levels required to reach a signal-to-noise of 3 per unit \AA in an integration time of 400 s. The flux for 3C273 is shown for reference.

$H_{ast}(\lambda)$ is the astigmatism height variation with wavelength and D is the dispersion (for *HUT*, *LIDOS*, and *FUSE*: 40, 25, and 1 \AA mm^{-1} respectively). $B(\lambda)$ is the background rate, which we model as the combination of the radiation-induced background, intrinsic detector dark counts and 3 kRayleighs of Lyman- α (typical of Lyman- α nightglow) filling the $10'' \times 300''$ slit of the spectrograph convolved with a measured scattering profile. Based on the orbital experience of *HUT*, each of these backgrounds contributes $\approx 0.5 \text{ cnts cm}^{-2} \text{ s}^{-1}$ far from the Lyman- α line core. The results are shown on the left of Figure 8. For the CCD the background is limited by the amplifier read noise ($5 \text{ e}^- \text{ rms}$) for short exposures and by the thermal dark current in the silicon (see Table 1) for long exposures. Lyman- α backgrounds in the CCD are only important for long exposures. The BEF of the *LIDOS* MCP channel is lower than *HUT* because they did not correct for astigmatism. It is lower than *FUSE* because the spectrum is less dispersed. Given enough observing time this instrument will be capable of seeing deeper than either *HUT* or *FUSE*. The expected flux limit yielding a signal-to-noise of 3 in 400 seconds is shown on the right of Figure 8.

5. DISCUSSION

The dual order spectrograph design presented here increases throughput by a factor of two. It provides a system redundancy in the primary science instrument that is desirable in the high risk environment of space-base missions. The design is flexible. It can be used with different detectors, as described herein, to extend the dynamic range of the instrument. It can also be used with dual MCP detectors to increase the sensitivity to low flux objects.

The dual order concept is not limited to Rowland circle spectrographs. We have studied dual order Wadsworth designs with astigmatism reduced by a parabolic toroidal figure and higher order aberrations reduced by curved ruling holographic solutions. The Wadsworth mounting with its single bounce is attractive as a high throughput spectrograph design. Mechanical collimators are required to reduce field-of-view confusion and airglow background, and because they are formed by stacks of plates with “lands” and “voids” they also reduce throughput. However, collimators have been made with a throughput as high as $\approx 66\%$,³² suggesting that far-UV dual order Wadsworth designs merit further study.

Astigmatism in the normal incidence mount ($\alpha = 0^\circ$) will always be higher than in the minimal astigmatism mount ($\beta = 0^\circ$).⁴ Although a toroidal figure can significantly reduce the astigmatism it does so at only one wavelength in each order. Growth of astigmatism away from the stigmatic point scales with the diffracted angle (β). To mitigate this problem and keep the spectral resolution fixed, designers should use a longer focal length and lower ruling density

We have shown how an electron impact excitation lamp can be integrated into a far-UV spectrograph without recourse to moving parts that could possibly block the primary optical path. We have been successful in decreasing the contrast between the bremsstrahlung continuum and line emission over that produced in our early experiments with Bayard-Alpert³³ (ion-gauge) tubes. The inclusion of this on-board source in far-UV spectrographs is expected to significantly

improve the quality of the spectral data product by allowing for in-situ wavelength calibration and correction of detector flat field variations.

We look forward in the future to presenting a more complete report on the operation of the electron impact lamp, the cryogenic and spectral performance of the δ -doped CCD, the imaging performance of the grating, and the overall performance of LIDOS.

ACKNOWLEDGMENTS

We wish to acknowledge the support of Shouleh Nikzad and Peter Deelman at JPL who supplied processing information and performed the delta-doping on the thinned SITE CCD. We would like to thank O. H. Siegmund for supplying the COS CsI QDE's. We would also like to thank SITE for identifying a lot of thinned CCD's suitable for delta-doping. This work is supported through NASA grants NAG5-5315 & NAG5-11456 to JHU.

REFERENCES

1. J. Flamand, F. Bonnemason, A. Thevenon, and J. M. Lerner, "Blazing of holographic gratings using ion-etching," in *Proc. SPIE Vol. 1055, p. 288, Raman Scattering, Luminescence and Spectroscopic Instrumentation in Technology, Fran Adar; James E. Griffiths; Jeremy M. Lerner; Eds., 1055*, pp. 288–+, July 1989.
2. G. H. Mount and W. G. Fastie, "Comprehensive analysis of gratings for ultraviolet space instrumentation," *Appl. Opt.* **17**, pp. 3108–3116, Oct. 1978.
3. S. R. McCandliss, E. B. Burgh, and P. D. Feldman, "Ultraviolet groove efficiency of a holographic grating: implications for a dual-order spectrograph," *Appl. Opt.* **40**, pp. 2626–2642, June 2001.
4. H. Noda, T. Namioka, and M. Seya, "Geometric theory of the grating," *J. Opt. Soc. Am.* **64**, pp. 1031–1036, 1974.
5. O. H. Siegmund, M. A. Gummin, J. M. Stock, D. R. Marsh, R. Raffanti, and J. Hull, "High-resolution monolithic delay-line readout techniques for two-dimensional microchannel plate detectors," in *Proc. SPIE Vol. 2006, p. 176-187, EUV, X-Ray, and Gamma-Ray Instrumentation for Astronomy IV, Oswald H. Siegmund; Ed., 2006*, pp. 176–187, Nov. 1993.
6. O. H. Siegmund, M. A. Gummin, T. Sasseen, P. N. Jelinsky, G. A. Gaines, J. Hull, J. M. Stock, M. L. Edgar, B. Y. Welsh, S. R. Jelinsky, and J. V. Vallergera, "Microchannel plates for the UVCS and SUMER instruments on the SOHO satellite," in *Proc. SPIE Vol. 2518, p. 344-355, EUV, X-Ray, and Gamma-Ray Instrumentation for Astronomy VI, Oswald H. Siegmund; John V. Vallergera; Eds., 2518*, pp. 344–355, Sept. 1995.
7. D. J. Sahnaw, M. A. Gummin, G. A. Gaines, A. W. Fullerton, M. E. Kaiser, and O. H. Siegmund, "On-orbit performance of the double delay line detectors for the Far Ultraviolet Spectroscopic Explorer," in *Proc. SPIE Vol. 4139, p. 149-162, Instrumentation for UV/EUV Astronomy and Solar Missions, Silvano Fineschi; Clarence M. Korendyke; Oswald H. Siegmund; Bruce E. Woodgate; Eds., 4139*, pp. 149–162, Dec. 2000.
8. J. B. McPhate, O. H. Siegmund, G. A. Gaines, J. V. Vallergera, and J. S. Hull, "Cosmic Origins Spectrograph FUV detector," in *Proc. SPIE Vol. 4139, p. 25-33, Instrumentation for UV/EUV Astronomy and Solar Missions, Silvano Fineschi; Clarence M. Korendyke; Oswald H. Siegmund; Bruce E. Woodgate; Eds., 4139*, pp. 25–33, Dec. 2000.
9. D. C. Slater, S. A. Stern, T. Booker, J. Scherrer, M. F. A'Hearn, J. Bertaux, P. D. Feldman, M. C. Festou, and O. H. Siegmund, "Radiometric and calibration performance results of the Rosetta UV imaging spectrometer ALICE," in *Proc. SPIE Vol. 4498, p. 239-247, UV/EUV and Visible Space Instrumentation for Astronomy and Solar Physics, Oswald H. Siegmund; Silvano Fineschi; Mark A. Gummin; Eds., 4498*, pp. 239–247, Dec. 2001.
10. J. B. McPhate, P. D. Feldman, S. R. McCandliss, and E. B. Burgh, "Rocket-borne Long-Slit Ultraviolet Spectroscopy of Comet Hale-Bopp," *ApJ* **521**, pp. 920–927, Aug. 1999.
11. J. Janesick, T. Elliott, T. Daud, J. McCarthy, and M. Blouke, "Backside charging of the CCD," in *Solid state imaging arrays; Proceedings of the Meeting, San Diego, CA, August 22, 23, 1985 (A87-10977 01-35). Bellingham, WA, Society of Photo-Optical Instrumentation Engineers, 1985, p. 46-79. NASA-supported research., 570*, pp. 46–79, 1985.
12. P. F. Morrissey, S. R. McCandliss, and P. D. Feldman, "Vacuum-ultraviolet quantum efficiency of a thinned, backside-illuminated charge-coupled device," *Appl. Opt.* **34**, pp. 4640–4650, Aug. 1995.

13. M. E. Hoenk, P. J. Grunthaler, F. J. Grunthaler, R. W. Terhune, M. Fattahi, and H. Tseng, "Growth of a delta-doped silicon layer by molecular beam epitaxy on a charge-coupled device for reflection-limited ultraviolet quantum efficiency," *Applied Physics Letters* **61**, pp. 1084–1086, Aug. 1992.
14. S. Nikzad, M. E. Hoenk, P. J. Grunthaler, R. W. Terhune, F. J. Grunthaler, R. Winzenread, M. M. Fattahi, H. Tseng, and M. P. Lesser, "Delta-doped CCDs: high QE with long-term stability at UV and visible wavelengths," in *Proc. SPIE Vol. 2198, p. 907-915, Instrumentation in Astronomy VIII, David L. Crawford; Eric R. Craine; Eds.*, **2198**, pp. 907–915, June 1994.
15. S. Nikzad, T. J. Jones, S. T. Elliott, T. J. Cunningham, P. W. Deelman, A. B. Walker, and H. M. Oluseyi, "Ultrastable and uniform EUV and UV detectors," in *Proc. SPIE Vol. 4139, p. 250-258, Instrumentation for UV/EUV Astronomy and Solar Missions, Silvano Fineschi; Clarence M. Korendyke; Oswald H. Siegmund; Bruce E. Woodgate; Eds.*, **4139**, pp. 250–258, Dec. 2000.
16. S. R. McCandliss, E. B. Burgh, and P. D. Feldman, "Flyable windowless calibration lamps for far-UV spectroscopy," in *Proc. SPIE Vol. 4139, p. 70-79, Instrumentation for UV/EUV Astronomy and Solar Missions, Silvano Fineschi; Clarence M. Korendyke; Oswald H. Siegmund; Bruce E. Woodgate; Eds.*, **4139**, pp. 70–79, Dec. 2000.
17. I. Kanik, G. K. James, and J. M. Ajello, "Medium-resolution studies of extreme-ultraviolet emission from CO by electron impact," *Phys. Rev. A* **51**, pp. 2067–2074, Mar. 1995.
18. J. M. Ajello, G. K. James, and D. E. Shemansky, "Cross sections for production of H(2p, 2s, 1s) by electron collisional dissociation of H₂," *ApJ* **371**, pp. 422–431, Apr. 1991.
19. J. M. Ajello, G. K. James, B. O. Franklin, and D. E. Shemansky, "Medium-resolution studies of extreme ultraviolet emission from N₂ by electron impact - Vibrational perturbations and cross sections of the c4-prime 1Sigma(+)u and b-prime 1Sigma(+)u states," *Phys. Rev. A* **40**, pp. 3524–3556, Oct. 1989.
20. J. M. Ajello and B. Franklin, "A study of the extreme ultraviolet spectrum of O₂ by electron impact," *J. Chem. Phys.* **82**, pp. 2519–2528, Mar. 1985.
21. D. E. Shemansky, D. T. Hall, and J. M. Ajello, "Electron impact excitation of H₂ - Rydberg band systems and the benchmark dissociative cross section for H Lyman-alpha," *ApJ* **296**, pp. 765–773, Sept. 1985.
22. J. M. Ajello, "The EUV spectrum of H₂O by electron impact," *Geophys. Res. Lett.* **11**, pp. 1195–1198, Dec. 1984.
23. D. Hall, D. E. Shemansky, V. Argabright, W. McClintock, W. Pryor, C. W. Hord, B. Franklin, J. Watkins, S. Srivastava, G. K. James, W. T. Simms, and J. M. Ajello, "Simple ultraviolet calibration source with reference spectra and its use with the Galileo orbiter ultraviolet spectrometer," *Appl. Opt.* **27**, pp. 890–914, Mar. 1988.
24. R. A. M. Keski-Kuha, J. F. Osantowski, H. Herzig, J. S. Gum, and A. R. Toft, "Normal incidence reflectance of ion beam deposited SiC films in the EUV," *Appl. Opt.* **27**, pp. 2815–, July 1988.
25. S. R. McCandliss, M. E. Martinez, P. D. Feldman, R. Pelton, R. A. Keski-Kuha, and J. S. Gum, "Design and fabrication of a 40-cm-diameter SiC-coated normal incidence telescope and spectrometer," in *Proc. SPIE Vol. 2011, p. 310-321, Multilayer and Grazing Incidence X-Ray/EUV Optics II, Richard B. Hoover; Arthur B. Walker; Eds.*, **2011**, pp. 310–321, Feb. 1994.
26. J. W. Kruk, T. M. Brown, A. F. Davidsen, B. R. Espey, D. S. Finley, and G. A. Kriss, "Final Astro-2 Calibration of the Hopkins Ultraviolet Telescope," *ApJS* **122**, pp. 299–329, May 1999.
27. D. J. Sahnou, S. D. Friedman, W. R. Oegerle, H. W. Moos, J. C. Green, and O. H. Siegmund, "Design and predicted performance of the Far Ultraviolet Spectroscopic Explorer," in *Proc. SPIE Vol. 2807, p. 2-10, Space Telescopes and Instruments IV, Pierre Y. Bely; James B. Breckinridge; Eds.*, **2807**, pp. 2–10, Oct. 1996.
28. "<http://www.trexenterprises.com/advanmat.html>," 2002.
29. W. G. Fastie and D. E. Kerr, "Spectroradiometric calibration techniques in the far ultraviolet - A stable emission source for the lyman bands of molecular hydrogen," *Appl. Opt.* **14**, pp. 2133–2142, Sept. 1975.
30. E. D. Palik, *Handbook of optical constants of solids*, Academic Press Handbook Series, New York: Academic Press, 1985, edited by Palik, Edward D., 1985.
31. "<http://fuse.pha.jhu.edu/support/guide/guide.html#INEFF>," 2002.
32. M. Melozzi and M. Fibbi, "Mechanical collimators for EUV spectrometers," in *New technologies for astronomy; Proceedings of the Meeting, Paris, France, Apr. 25, 26, 1989 (A90-37976 16-89)*. Bellingham, WA, Society of Photo-Optical Instrumentation Engineers, 1989, p. 118-125. Research supported by the Universita di Trieste., **1130**, pp. 118–125, Sept. 1989.
33. R. T. Bayard and D. Alpert, "Extension of the low pressure range of the ionization gauge," *Rev. Sci. Instr.* **21**, p. 571, 1950.